Shock Waves (2025) 35:739–758
https://doi.org/10.1007/s00193-025-01245-1

ORIGINAL ARTICLE

Markers of nonlinearity in the interaction of an acoustical shock with a ramp

S. Deleu[1] · R. Gojon[1] · J. Gressier[1]

Received: 3 May 2024 / Revised: 30 July 2025 / Accepted: 31 July 2025 / Published online: 16 October 2025

Abstract
The various nonlinear effects attributed to the propagation and the interaction of an acoustical shock with a ramp are investigated in this paper. The prevalent use of linear approximations in acoustic source localization techniques is a limitation to the accurate localization prediction required in military contexts. To address this issue, our approach seeks to identify different markers of nonlinearity within the acoustical shock wave framework, enlightening their reflective characteristics and the underlying physics. This study investigates the complex interaction between a high-amplitude acoustic pulse and a ramp, focusing on the reflection patterns of an acoustical shock. In particular, the single parameter used for the reflection pattern assessment is enhanced beyond its conventional formulation. The development of an irregular reflection detection algorithm is presented and serves as a fundamental component for a spectral analysis operating Fourier decomposition enabling a reflection-type classification solely based on time-signal measurements. This work contributes to the broader understanding of acoustic shock interactions and offers insights into improving the accuracy of source localization techniques, especially in situations where linear assumptions may prove to be limited.

Keywords Acoustical shock · N-waves · Shock reflection regimes · Transition parameter · Nonlinear interaction

1 Introduction

Impulse sound sources, often associated with explosions and sniper fire, are of particular interest in military applications, underlining the importance of acoustic source detection. The generated signal takes the form of a propagating acoustical shock, generally described as an N-wave, with front and rear shocks separated by a linear pressure decay. In those cases, the near-source pressure–time waveform is often not as simple as an N-wave and reaches this ideal shape only far from the source. This occurs because high-amplitude regions of a strong acoustic signal travel faster. This dispersion of the signal leads to its distortion and eventually to a shock formation. The same opposite behavior is observed in low-amplitude regions. Those N-waves either arise from a high-amplitude signal propagation as previously described, or, in scenarios such as a bullet Mach wave or a muzzle blast, the N-wave forms directly at the emission point. To quantify the strength of acoustical shocks, the acoustic Mach number M_a, defined as the ratio of the acoustic velocity v_a over the ambient sound speed c_0, is used. This work exclusively presents 2D planar representations of such acoustical shocks. Their reflection is performed onto smooth and perfectly reflecting surfaces and their propagation in homogeneous and quiescent media. In particular, the smoothness of the surface is important, as roughness can delay the formation of a peculiar normal shock under certain conditions called Mach stem and reduce its height [1, 2]. The adoption of a 2D planar wave results from the magnitudes comparison of pressure decays due to nonlinearities and to geometrical effects (Appendix 2). This choice seems sufficient to represent the physics of interest while simplifying the number of parameters in order to enhance focus on nonlinear effects.

In the process of identifying the exact position of an acoustic source, multiple methods can be found to be effective with errors on the position varying from about ten meters [3] down to a few centimeters [4] (To compare the accuracy of a given system, the error range needs to be normalized with the size of the domain studied). Several techniques assess the acoustic source location with different accuracy

Communicated by C.-Y. Wen.

✉ S. Deleu
deleu.samuel1@gmail.com

[1] ISAE SUPAERO, Université de Toulouse, 10 Avenue Edouard Belin, 31400 Toulouse, France

levels. For instance, Cheinet et al. [3] developed a pragmatic process for acoustic source localization (ASL) during urban explosions. Their time-matching technique optimizes computational time within an accuracy range of a few tens of meters, relying on a priori terrain knowledge. Explosion simulations are performed for each possible position on the mapped terrain, recording signals at pre-defined microphone locations. A database is built from these simulations, and the real-time signals from an actual explosion are compared to this database. The closest match identifies the source position.

The most accurate approaches for acoustic source localization are typically used in indoor systems, where acoustics are usually linear and nonlinearities are minimal due to small-scale configurations and weak perturbation signals (Liu et al. [5]). The time-reversal acoustics method [6], for instance, refocuses acoustic waves at their source by turning receiving sensors into emitters of time-reversed signals. This relies on time-reversal invariance, assuming an isentropic signal. However, nonlinear waves can limit this method. Tanter et al. [7] observed that while energy in harmonic components can return to the fundamental during time reversal, this holds only until shock formation, marking the method's limit.

Among linear-based localization methods, ray-tracing technique or time of arrival [8] can be listed. The first uses linear reflection properties to describe the path of the wave, which is a strong hypothesis not suitable for the reflections of high-amplitude waves [9, 10]. The second is the simplest and most widely used method for source localization and is used under the linear propagation properties assumption.

Most of these methods neglect nonlinear effects in propagation, and most importantly, none of them account for nonlinear interactions (diffraction or reflection).

Von Neumann [11] investigated the reflection patterns and theoretically predicted the apparition condition for the triple point. The solution of the non-standard three-shock theory (3ST) yields a von Neumann reflection (vNR) which was first introduced by Colella and Henderson [12]. When it comes to weak acoustical shocks, 3ST fails to predict the existence of a three-shock pattern [12] in which three plane shocks and a plane contact discontinuity separated by constant states meet at the triple point [13]. However, numerical and experimental studies exhibiting this phenomenon exist [14, 15]. The regime of reflection is known as the von Neumann reflection whereas the discrepancy between theoretical results from 3ST and experimental/numerical ones is known as the von Neumann paradox.

This study seeks to explore the nonlinear effects involved in the interaction between an acoustical shock and a ramp, and to introduce a simple marker for identifying nonlinear behavior in urban acoustics. This paper uses high-order numerical simulation results to assess the reflection type (detailed in Sect. 3). It investigates the reflection transition limit and suggests a spectral decomposition to evaluate it.

The article is organized as follows. Section 2 introduces the chosen numerical method to propagate discontinuities. Section 3 analyzes the case of a step shock reflection with the introduction and discussion of the transition parameter a. A triple-point detection algorithm is detailed and used to compare the reflection transition limits with the algorithm results in the case of a step shock. Section 4 extends the triple-point detection to N-waves acoustical shocks. Section 5 provides a conclusion.

2 Computational simulations with IC3 solver: methodology and dataset construction

In this section, the features of the employed numerical method are detailed before describing how the resulting database was constructed. The entire collection of simulation results provided in this article has been obtained using the IC3 (read "Ice Cube") solver, a massively parallel high-order solver developed and maintained at ISAE-SUPAERO. Results are built up on the developments performed in Lamouroux et al.'s work [16] that consisted of implementing high-order spectral difference methods and a high-order compact limiter. The latter enables the propagation of discontinuities by minimizing oscillating behaviors in the polynomial reconstruction of the flow variables.

The spectral difference method (SD) is used here to solve the 2D Euler equations. It is a class of high-order methods generally used to solve hyperbolic systems. The specificity of the SD method lies in the discretization of the elements used to reconstruct the fluxes. Each element contains several nodes in each direction. The reconstruction of the solution uses a polynomial approximation of order p. A pth-order SD method in 2D would require p^2 solution points and $2 \times (p+1) \times p$ flux points. Solution and flux points are two sets of points that enable the definition of the Lagrange interpolation polynomials, necessary in the construction of SD schemes. The reader can refer to the extended work of Liu et al. [17] for a deeper understanding of SD schemes. The SD scheme used in this work is of order 3.

When solving nonlinear systems such as conservation laws, solutions can develop into discontinuities. Since high-order methods such as SD are based on polynomial approximations, one can understand the challenge of approximating a discontinuity with such a numerical scheme using oscillatory functions. The consequence is then the appearance of spurious oscillations at the discontinuity. The main purpose of the limiter lies in the limitation of those oscillations. A specific limiter—SWeP (spatially weighted projections) Limiter—is used to respect the stencil compactness as

required to maintain good computational efficiency of the high-order spectral methods.

The SWeP limiter has been developed for SD schemes and implemented in IC3 [16]. To do so, the general strategy deployed is to consider a "direct" reduction of the polynomial degree, as opposed to an "a posteriori" interpolation method that can also be found to address the problem. The triggering of the reduction is based on the evaluation of the quantity $s_e = \log_{10}(\hat{u}_k^2/||\hat{u}||_2^2)$, where $\hat{u} = \sum_{k=1}^{n} \hat{u}_k \phi_k^L$ is the polynomial approximation of the solution (with ϕ_k^L a Lagrange (L) polynomial function and $||\hat{u}||_2^2 = \sum_{k=1}^{n} \hat{u}_k^2$). The quantity s_e assesses the relative energetic significance of the high-frequency content of the polynomial, which is responsible for the oscillatory nature of the solution that is intended to be damped. Therefore, the solution is projected—using specifically developed mathematical objects called projectors—in a new base of polynomials of order $p - r$, r being the order of reduction applied to the solution ($r = 1$ in the development of the SWeP limiter used in IC3, as greater order of reduction would need another complete evaluation and construction of projectors) and p the order of the polynomial being reduced. A cell within the computational domain can exist in two distinct states: it may either contain a discontinuity or not. Before applying any limitation, the limiter must determine whether a cell bears a discontinuity or not. The detection strategy for the SWeP limiter is adapted from the one developed by Persson for artificial viscosity [18], where the evaluation of the numerical viscosity corresponds to the computation of a marker for regions requiring consideration of the term responsible for diffusion. In Lamouroux et al.'s work, this term is called α^{1D}. If a cell has $\alpha^{1D} > 0$, then it contains a discontinuity. The SWeP limiter is not activated in a binary manner, but is progressively activated by a weighting function α^{1D} directly computed from s_e [16]. To be a bit more specific, the limiter is proportionally applied (which can be seen as a blending) onto the original polynomial (of order p) and the reduced polynomial (of order $p - r$) in such a way that an α^{1D} coefficient is applied on polynomials of order p and $(1 - \alpha^{1D})$ is applied on polynomials of order $p - r$ [16]. The limiter operation can be summed up in two main stages: detect discontinuities and locally reduce the polynomial order of the solution.

A significant amount of numerical simulations are performed with the intent of building a dataset from which analysis will be done in the next sections. The analysis will be based on different signals recorded using numerical probes placed inside the computation domain as presented in Fig. 1. To obtain these signals, different plane waves interacting with a wedge will be considered. Both the acoustic Mach number M_a—recalled as the ratio between the acoustic velocity over the ambient sound speed—and the angle of the wedge θ_w are taken as control parameters for the dataset construction.

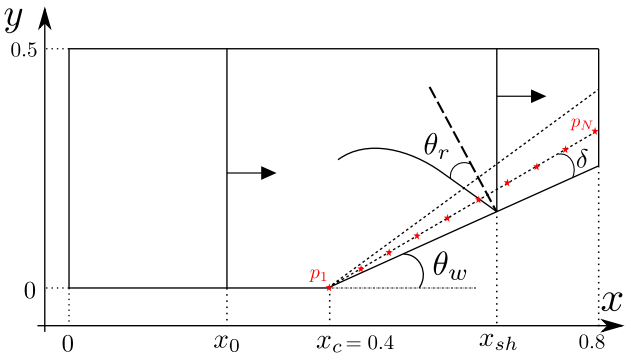

Fig. 1 Domain representation of the location of the probes along a line of a given angle δ from the wedge surface with x_0 the starting shock position, x_c the corner position, x_{sh} the shock position, and coordinates in meters

Table 1 Dataset summary for both investigated cases

Cases	Step shock	Plane N-wave
Number of cases	368	575
Range in M_a	$[10^{-4}, 10^{-1}]$	$[5 \cdot 10^{-4}, 6 \cdot 10^{-2}]$
Range in θ_w	$[2°, 40°]$	$[2°, 40°]$

A total of 368 combinations of (θ_w, M_a) are conducted for step shock cases (refer to Sect. 3), and this number increases to 575 for 2D planar N-waves, keeping the wavelength constant not to increase the parameter space (refer to Sect. 4). The selection of these specific parameter values is driven by the need to span an acoustically relevant range within the (θ_w, M_a) domain. Table 1 summarizes the performed cases and ranges. Please note that the starting shock position is $x_0 = x_c - 0.05(\text{m})$ for the step shocks and that the initial position of the N-wave rear shock is $x_0 = x_c - 0.2(\text{m})$.

In Sect. 3.3, t_{ref}—time at which results are provided—is chosen to ensure a correct Mach stem resolution and also to get enough information from the chosen recording probe. Indeed, the auto-similarity of the step shock reflection enforces that the greater the distance of propagation, the greater the Mach stem. Therefore, t_{ref} must be calibrated for the wave to pass the chosen probe and also for the wave to avoid hitting the right boundary of the domain, which would result in the creation of a reflecting wave (see Fig. 1). In the remaining text, $l_{ref} = c_0 \cdot t_{ref}$ is the approximate shock position.

A grid convergence study using the Richardson extrapolation method is provided for three different grid spacings in Appendix 1. The result confirms that the grid size choice is sufficient for an accurate prediction of acoustical shock propagation.

3 Characterizing step shock reflection patterns

Nonlinearity in acoustic wave propagation causes signal distortion. The second most important nonlinear feature lies in the reflection pattern of the acoustical shock. In this section, our attention will be focused on a simplified acoustical shock namely the step shock. A step shock is a discontinuity whose 1-D profile matches the step function. Physically, it is a discontinuity behind which the fluid state is changed and remains uniform. Since acoustic signals generally oscillate around a certain value, the step shock's inherent constant downstream flow makes it somewhat non-realistic in the acoustics framework but its simplicity makes it a suitable model for studying and analyzing acoustical shock interactions. When discussing source localization, understanding the nature of reflections is crucial. Whenever the incident and reflected shocks meet at a point attached to the reflecting surface, the reflection is classified as a regular reflection (RR). A representation of the same reflection regime (RR) is given in both steady and unsteady framework in Fig. 2 which explains how an unsteady phenomenon can be reduced to a quasi-steady state allowing the use of Rankine–Hugoniot relations valid across a steady shock. In the case of a nonlinear regular reflection (NLRR), the reflected angle differs from the incident angle, while the shock remains attached to the surface [10]. Irregular reflection (IR) occurs when the maximum flow turning angle at a given Mach number is less than the wedge angle. Here, the reflected shock cannot turn the flow parallel to the wedge surface, causing the meeting point between the incident shock and reflected shock to detach from the surface, thus creating a Mach stem and forming a triple point. Whether it is a linear regular reflection (RR), a nonlinear regular reflection (NLRR), or a von Neumann reflection (referred to as IR in the context of acoustical shocks), they result in distinct pressure signals. These pressure differences can lead to errors during the back-propagation stage of localization, especially considering that linear reflections are predominant in typical source localization scenarios [19, 20]. In the literature, a parameter a provides information about the reflection regime.

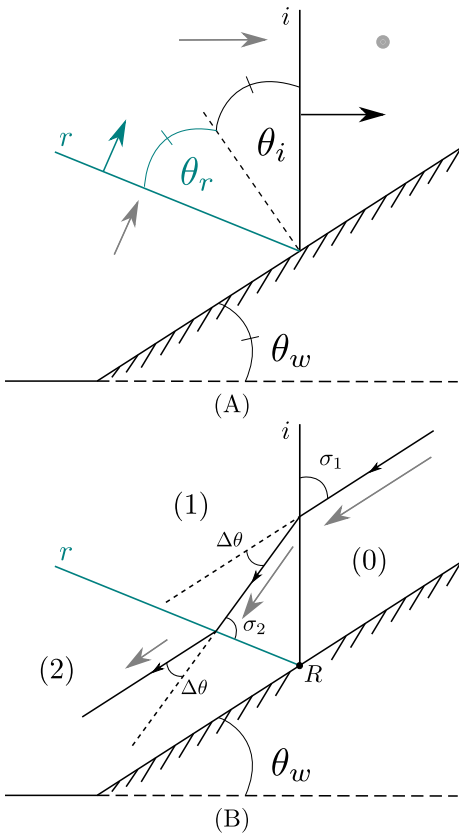

Fig. 2 **A** RR of a shock in the lab frame of reference (unsteady representation); the black arrow is the shock speed, the gray arrows are the shock-induced flow convection. **B** represents the same RR in the shock frame of reference reproducing the unsteady reflection in a quasi-steady state and allowing the use of Rankine-Hugoniot relations. Gray arrows represent the flow speed while the black line would be the trajectory of a fluid particle across this shock system

3.1 Detachment conditions

3.1.1 Parameter *a*

The reflection-type determination can be achieved using a certain parameter: a. The first derived formula for a was introduced by Tesdall and Hunter on their self-similar approach of the weak shock solution [14]. This formulation was used by Hunter and Brio [21] and Zakharian et al. [22] for their study on the von Neumann paradox. Another expression can be found in Skews and Ashworth [15]. The formulation of a used in this work comes from the derivation of nonlinear acoustics paraxial equations (the KZK equations, for instance [23]). This formulation has been widely used for the description of the reflection-type transition in the case of acoustical shocks [24–27]:

$$a = \frac{\sin\theta_\mathrm{i}}{\sqrt{(\gamma+1)M_\mathrm{a}}} \tag{1}$$

with θ_i being the angle of incidence of the incident shock, within a validity range of $\theta_\mathrm{i} < 15°$. This range is based on the assumption that the paraxial equation, from which a is derived, is valid for wave propagation directions that deviate by less than 30°. In this range, the error in the dispersion relation remains below 1% according to Baskar et al. [10].

The limit between regular and irregular reflection was determined by a fixed (critical) value of the parameter a that is $a_\mathrm{c} = \sqrt{2}$ [28]. The parameter a compares the effects of reflection and diffraction associated with the grazing angle to the effect of nonlinearities [10]. Irregular reflection is

expected for $a < a_c$ and regular reflection for $a > a_c$ under grazing incidence conditions. It is often referred to as the critical (or transition) parameter in the literature [10, 12]. The parameter aims at gathering a two-degree-of-freedom problem that is defined with both θ_w and M_a, respectively, the wedge angle and the acoustic Mach number of the propagating shock. Even though different definitions for the dimensionless parameter can be found in the literature, each is mainly based on the general assumption that [10, 21]:

$$\theta_i = \mathcal{O}\left(\sqrt{M_s - 1}\right) \quad \Leftrightarrow \quad \theta_i = \mathcal{O}\left(\sqrt{M_a}\right) \tag{2}$$

where θ_i corresponds to the incident shock angle with $\theta_i = \theta_w$ in our case (see Fig. 2). The asymptotic evaluation of the expression linking the shock Mach number M_s—defined as the ratio between the shock speed and the ambient sound speed—to the acoustic Mach number M_a leads to the following:

$$M_a = \frac{2}{\gamma + 1}(M_s^2 - 1) \approx \frac{4}{\gamma + 1}(M_s - 1) \tag{3}$$

which states that $\mathcal{O}(M_a) = \mathcal{O}(M_s^2 - 1) \approx \mathcal{O}(M_s - 1)$ and justifies the right-hand-side relation in (2).

3.1.2 Reflection transition limits

In his PhD thesis, Mouton [29] presented a detailed shock analysis determining the domain boundaries of shock reflection in a *steady flow*. In particular, he developed analytical solutions for boundaries between different solutions whenever it was possible and gave limiting values for these boundaries. He used $(\sigma_1,\ M_0)$ (see Fig. 2B) as parameters to identify specific regions for different types of reflections to occur, with $\sigma_1 = \frac{\pi}{2} - \theta_w$ the shock angle and M_0 the upstream Mach number. This section draws inspiration from Mouton's work in steady flows to find the detachment condition and identify the reflection region for a propagating shock (pseudo-steady, see Fig. 2A) in the parameters of interest $(a,\ \theta_w)$, with a the parameter introduced in Sect. 3.1.1.

The detachment condition for a given Mach number represents the incident shock angle at which the maximum deflection angle is achieved for the reflected shock, namely σ_D. This means that beyond this angle, the flow turning angle of the reflected shock is beyond its maximum permissible value, causing the reflection to be of another type than a RR. The intersection of the incident and reflected shock is then detached from the wall and a Mach stem is created.

To find the incident shock angle at the detachment condition, σ_D, the incident shock flow deviation angle $\Delta\theta$ and the maximum flow deflection angle of the reflected shock must be the same for any couple $(\sigma_1,\ M_0)$. The Mach number M_1 behind the leading oblique shock at this condition is

$$M_{1,D} = M_1(M_0,\ \sigma_D) \tag{4}$$

Therefore, the deflection angle $\Delta\theta$ must satisfy the following condition:

$$\Delta\theta(M_0, \sigma_D) = \Delta\theta\Big(M_{1,D},\ \sigma^{\theta_{max}}\left(M_{1,D}\right)\Big) \tag{5}$$

with $\sigma^{\theta_{max}}$ the shock angle value at which the reflected shock deviation angle reaches its maximum value θ_{max}. This is equivalent to saying that the deflection angle σ_D occurring at the incident shock should be equal to the maximum deflection angle admissible by the induced reflected shock. Equation (5) is a relation between σ_D and M_0. In a steady flow, solving the system for σ_D gives a limit in the $(\sigma,\ M_0)$ domain above which any given combination of Mach and shock angle means that RR is impossible (see Figure 2.28 on page 38 in Mouton's work [29]).

3.1.3 Detachment criterion a_D in the $(a,\ \theta_w)$ domain

In the previous Sect. 3.1.2, the detachment condition is introduced. The given shock angle σ_D—responsible for the flow to deviate more than the reflected shock admissible deviation θ_{max}, therefore inducing an IR—can be found with the properly constrained Rankine–Hugoniot relations (4). This equation—derived by Mouton and available on page 21 of his PhD thesis [29]—allows us to determine σ_D for a steady-state flow.

The step shock reflection is a quasi-steady phenomenon. Therefore, there exists an equivalent steady-state flow condition *in the wave frame of reference* for each given couple $(\theta_w,\ M_a)$. The resolution of (4) for σ_D determines the wedge angle for the detachment condition $\theta_{w,D} = \frac{\pi}{2} - \sigma_D$.

Knowing $\theta_{w,D}$, it is possible to plot a_D, defined here as the parameter a obtained with the detachment condition detailed in Sect. 3.1.2. The expression of a_D as a function of $\theta_{w,D}$ is:

$$a_D = f(\theta_{w,D}) = \frac{\sin\left(\theta_{w,D}\right)}{\sqrt{(\gamma + 1)M_{a,D}}} \tag{6}$$

with $M_{a,D}$ expressed using the left side of (3). The shock Mach number M_s in (3) can be written as a function of the upstream flow Mach number M_0 and the shock angle σ_1 as $M_s = M_0 \sin\sigma_1$ which for $\sigma_1 = \sigma_D$ yields:

$$M_{a,D} = \frac{2}{\gamma + 1}\left(M_0^2 \sin^2\sigma_D - 1\right) \tag{7}$$

It is important to note that $\theta_{w,D}$ is directly linked to the shock angle at which the detachment occurs σ_D. Each couple $(\theta_{w,D},\ M_{a,D})$ is uniquely determined as both depend on σ_D.

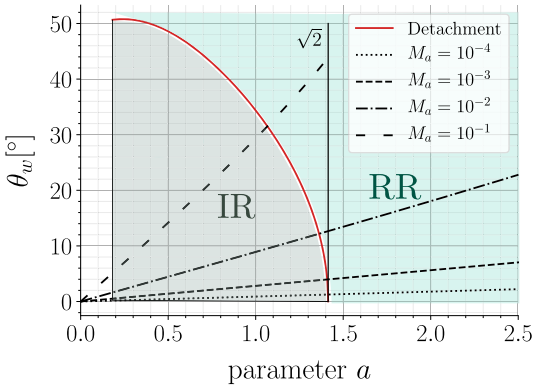

Fig. 3 Detachment condition limit a_D (in red) in the set of parameters (a, θ_w) along with constant acoustic Mach numbers (in black) and $a_\mathrm{c} = \sqrt{2}$

Therefore, when varying θ_w at the acoustic Mach number in the detachment condition $M_{\mathrm{a,D}}$, only a single value of θ_w will match the detachment condition from which a_D will be retrieved using (6). This is how a_D can be plotted in the (a, θ_w) domain (see Fig. 3) as well as in the (M_a, θ_w) domain (as presented in red in Fig. 9).

Results for the a_D value are presented in Fig. 3. The validity of the formulation of a_D is subjected to the γ value being maintained here to $\gamma = 1.4$ typical for diatomic gases. The first assertion from Fig. 3 is that, for grazing angles, the detachment condition is asymptotically equal to the value of $a_\mathrm{c} = \sqrt{2}$ generally used in the literature as seen in Sect. 3.1.1:

$$\lim_{\theta_\mathrm{w} \to 0} a_\mathrm{D} = \sqrt{2} \tag{8}$$

This value, as it is derived from the paraxial equation, is certainly valid for grazing angles. However, as shown in Fig. 3, there is an influence on the value of a for greater θ_w values, with a being over-estimated for greater angles compared to $a_\mathrm{c} = \sqrt{2}$. In Fig. 3, the detachment condition (red solid line) is plotted in this (a, θ_w) domain, along with the different corresponding constant acoustic Mach number of $M_\mathrm{a} = 10^{-4}$, $M_\mathrm{a} = 10^{-3}$, $M_\mathrm{a} = 10^{-2}$, and $M_\mathrm{a} = 10^{-1}$. More specifically, following lines of iso-Mach number M_a, it appears that from M_a slightly above 10^{-3} and below 10^{-2} the difference between a_D and $a_\mathrm{c} = \sqrt{2}$ becomes non-negligible which constrains the use of $a = \sqrt{2}$ to $M_\mathrm{a} < 10^{-3}$. Equivalently, when trying to figure out when discontinuous waves propagating with an acoustic pressure $p_\mathrm{a} > 150$ Pa are likely to detach, it seems preferable to use the developed limit a_D instead of the standard limit a typically set at a value of $a_\mathrm{c} = \sqrt{2}$.

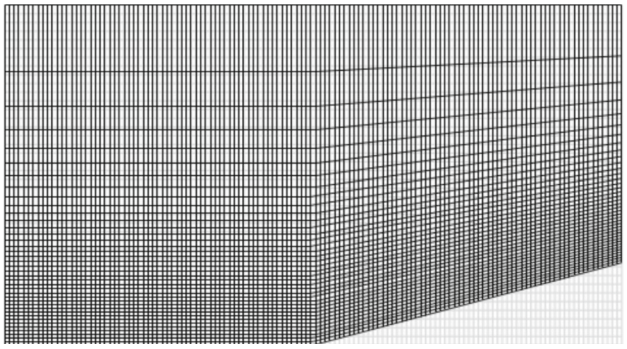

Fig. 4 Representation of the transformed 2D mesh (black) on top of the non-distorted uniform mesh (light gray) for a wedge angle of $\theta_\mathrm{w} = 20°$; one point out of 10 is plotted in both directions

3.2 Validation of the numerical approach

The simplest way to create a corner with a potential variable angle is to twist an existing uniform mesh. To do so, a 2D grid (see Fig. 4) is constructed with an automated tool that transforms an orthonormal Cartesian mesh into a mesh adapted to the problem through a bijective analytical function. Given that the reflective structure originates from the reflective boundary, the mesh becomes finer as it gets closer to the boundary. The refining law follows an arc-tangent function, while the mesh in the x-direction remains uniform. The morphing of the mesh and its adaptability is crucial in our study due to the necessity of simulating a diverse array of configurations (as presented in Table 1). The left boundary condition is set as an inlet where the inflow condition corresponds to the state observed behind a normal shock of intensity M_a. On the right side of the shock, the fluid is at rest with $P_0 = 10^5$ Pa. The upper, lower, and right walls are considered to be perfectly plane and infinitely rigid. Consequently, the shock will consistently strike the upper boundary at a perpendicular angle, and the simulation duration will not extend beyond the moment when the shock interacts with the right side of the domain. Consequently, both the upper and right walls will not influence the wave propagation nor the reflection phenomenon occurring at the corner.

A good way to assess the code validity in reproducing the studied physics is to observe the different reflection patterns caused by the interaction between the incident shock and the corner, as it is performed in this section. In their thorough numerical analysis, Baskar et al. [10] suggested critical values of the parameter a in the case of a step shock for the transition from one reflection regime to another (see Sect. 3.1.1).

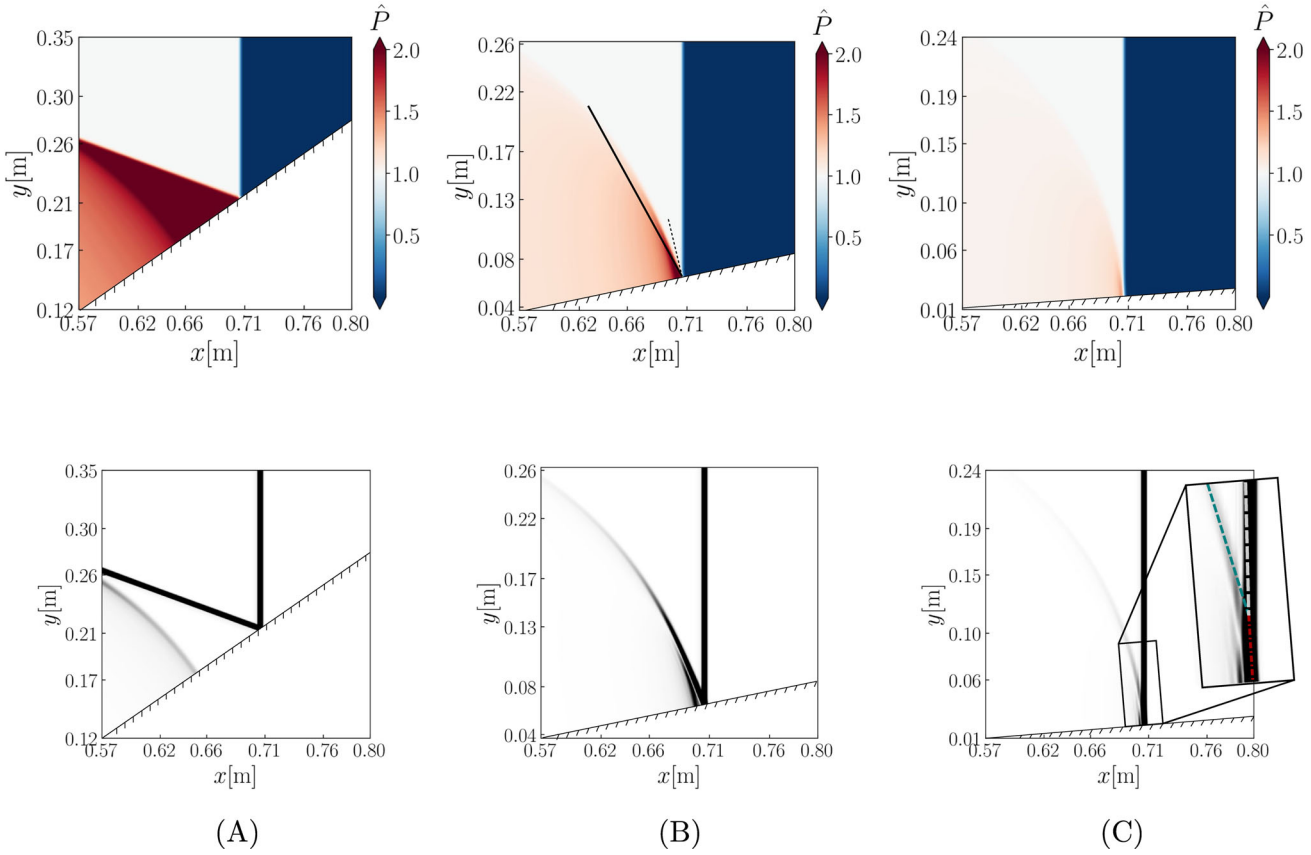

Fig. 5 Simulation results for the propagation of a step shock onto a wedge of angle **A** $\theta_w = 35°$, **B** $\theta_w = 12°$, and **C** $\theta_w = 4°$ for an acoustic Mach number $M_a = 3 \cdot 10^{-3}$. The top is the pressure color map, the bottom is the corresponding numerical schlieren (or density gradient) enhancing the visible wave reflection pattern

Results presented in Fig. 5 give the pressure field (upper figures) for different reflection angles, as well as their numerical schlieren (lower figures). The results were obtained using the same value of the acoustic Mach number $M_a = 3 \cdot 10^{-3}$ at a non-dimensional time of t_{ref}. This specific time corresponds to when the pressure field is visualized and ensures that the wave structure is adequately resolved by the mesh to accurately capture various reflection patterns in the case of a step shock. The mesh size is $\Delta x = 6 \cdot 10^{-4}$ m. It is worth noting that the value of t_{ref} may vary when examining N-waves (as discussed in Sect. 4.2).

The pressure field is depicted using the normalized pressure $\hat{P}$, which characterizes the relative pressure of the disturbance defined as $p_a = P - P_0$, where P is the actual pressure and P_0 is the ambient pressure. The expression for the normalized pressure is as follows:

$$\hat{P} = \frac{P - P_0}{P_{ith} - P_0}, \quad \text{with } P_{ith} = \left[\left({M_s}^2 - 1 \right) \frac{2\gamma}{\gamma + 1} + 1 \right] P_0 \tag{9}$$

where M_s is the shock Mach number and P_{ith} is the theoretical pressure encountered behind a normal shock with a Mach number M_s. Thus, normalized pressure considers the change in the pressure disturbance value p_a compared to the pressure that is typically observed behind a normal shock.

For each case presented in Fig. 5, the schlieren gives a better visualization of the reflection structure, while the pressure field gives information on the different values obtained behind both incident and reflected shocks. In Fig. 5, the only criterion responsible for the different reflection patterns is the wedge angle variation (iso-Mach simulations). Figure 5A and B shows their point of reflection well attached to the surface, which leads to the claim that both reflections are regular. The black line in Fig. 5B shows what the reflected shock would be if the reflection was specular, i.e., linear. As observed in Baskar et al. [10], the angle of incidence is different from the angle of reflection in Fig. 5B which indicates a regular nonlinear reflection (NLRR). In contrast, Fig. 5A indicates a regular linear reflection (RR) as both angles are equal. For these configurations, the values obtained from a are, respectively, $a = 6.76$ and $a = 2.45$. Figure 5C indicates a von

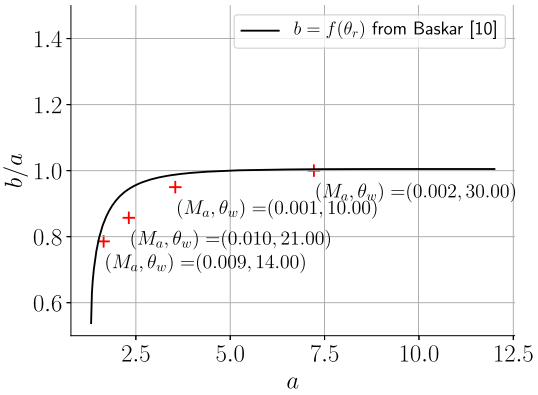

Fig. 6 Comparison of the obtained values of $b = f(\theta_r)$ for different cases, to the expression given in Baskar et al. [10]

Neumann reflection: the incident and reflected shock meet above the reflecting surface with the presence of a Mach stem, acknowledging the irregular behavior. For this case, parameter a is equal to $a = 0.82$. The transition from one reflection to another follows a certain value of a. Those values were indicated by Baskar et al. [10]. For $a > 5$, reflection is a linear RR while NLRR occurs for $\sqrt{2} < a < 5$. With $a < \sqrt{2}$, the reflection is considered irregular. Following Sect. 3.1.1, each value of a is consistent with the literature. The numerical results presented in Fig. 5 agree with what is expected considering the reflective nature of a step shock.

A simple relation between incident and reflection angles for NLRR was given in Baskar et al. (5.6), and a comparison with our simulation results is performed in Fig. 6. The parameter b is defined in Baskar et al. similarly to the parameter a but using reflected angle instead of incident angle. The different crosses represent different simulated cases for which the reflected angle has been measured. The highest discrepancy is observed for highest M_a and relatively high angle, which is coherent with the paraxial approximation of Baskar et al. [10] limited to small M_a and angles below 15°. The general behavior is well retrieved, validating the results.

3.3 Algorithm for the reflection-type determination

The determination of an IR can be done through the observation of a Mach stem in the reflection pattern. In the opposite case (no visible Mach stem), the reflection is of irregular type. This section presents a convenient way to know whether a Mach stem is formed or not: find the coordinates of the intersection of the incident and reflected shocks and estimate whether it belongs to the surface or not. If it does, the flow is sufficiently deviated by the reflected shock, indicating the presence of a RR. However, when the estimated point of intersection is located above the surface, it is proof of triple-point existence. Thus, the detachment conditions are met and the reflection is of irregular type (IR).

Because of the homothetic property of the simulation, the Mach stem formation starts theoretically infinitely close to the surface. Having the Mach stem length below a single-cell height makes its detection impossible from the start, requiring the definition of a numerical threshold. The minimum indicated value for the Mach stem height corresponds to the measured shock thickness $\kappa = 1.5 \cdot 10^{-3}$ m (which is equivalent to three mesh cells) in our numerical studies. This measurement will help us discriminate the reflection types. Indeed, any detected triple point above the surface but below the normalized value $\kappa^* = \kappa / l_{\text{ref}}$ would be considered as attached to the surface, giving rise to a RR detection. It is crucial to emphasize that reducing the minimum value of κ^* by an order of magnitude, i.e., $\mathcal{O}(\kappa^*/10)$, does not alter the drawn conclusions or the Mach stem height values. Therefore, the selected lower limit remains appropriate.

Among the several ways to numerically find the triple point, the retained method is the following. First, we need to get a spatial distribution of the pressure along several straight lines from the corner position $(x_c, y_c) = (0.4\text{ m}, 0\text{ m})$ up to the right domain boundary. Starting from the surface and increasing the angle δ between each line, the pressure will continuously be plotted for each δ value, in such a way that $\delta \in [\theta_w, \theta_w + 20°]$ as it is depicted in Fig. 1. Providing that the δ increment remains below the Mach stem length, the lines will necessarily cross the triple-point region if any. Therefore, the pressure distribution will vary from one shock front—when located in between the surface and the triple point—to two shock fronts whenever the δ angle is beyond the triple point. Eventually, to be able to differentiate a RR from an IR, the detection of a point will be performed to determine whether this point belongs to the surface of the wedge (RR) or not (IR).

The upper part of Fig. 7A gives an example of the pressure plots for the case $(M_a,\ \theta_w) = (8 \cdot 10^{-3},\ 3.5°)$ along a given line $\delta = 28°$. Below is the signal derivative plotted to find the incident and the reflected shock position. The shock being a discontinuity, it is numerically represented by high gradients: the greatest values of $\mathrm{d}P/\mathrm{d}x$ represent the shock position along the δ line. A threshold value $h_{\text{detection}}$ is determined as a fraction of $\max(\mathrm{d}P/\mathrm{d}x)$ to adapt to different $(\theta_w,\ M_a)$ couples and not to be readjusted for each investigated case. However, this precaution does not prevent peaks from being ill-determined in some cases, especially for low Mach number values. A value of $h_{\text{detection}} = 0.02\,(\max \mathrm{d}P/\mathrm{d}x)$ has been found to give satisfactory results. With increasing δ line value, both incident and reflected shock curves are retrieved. Then the shock curves are extrapolated to find their intersection. The extrapolation process involves a first-order fitting for the incoming shock, given its straight shape, and a second-order fitting for the reflecting shock, which is typically curved. A visual representation of this process can be seen in Fig. 7B. On each plot, the intersection of the extrapo-

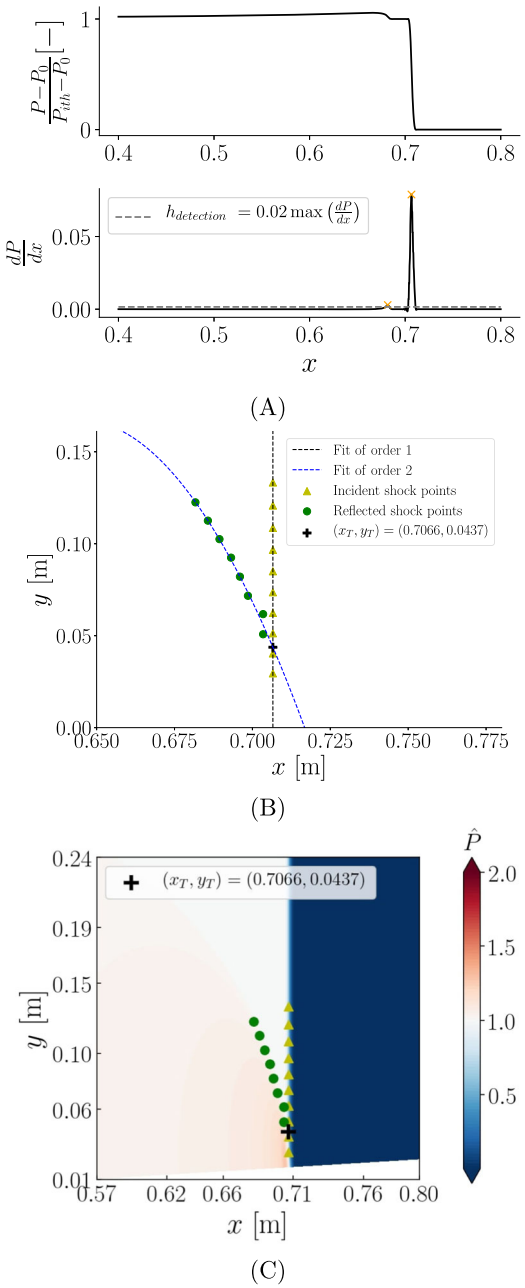

Fig. 7 Intersection point determination steps for $(M_a,\ \theta_w) = (8 \cdot 10^{-3},\ 3.5°)$. **A** The dimensionless pressure and its derivative along line $\delta = 28°$; **B** the intersection $(x_T,\ y_T)$ of the extrapolation of order 1 (i) and 2 (r); **C** the superposition of $(x_T,\ y_T)$ and determined peak position on top of the pressure distribution $\hat{P}$ in the domain

lated position of the incident (black dotted line) and reflected shock (blue dotted line) is visible and identified as $(x_T,\ y_T)$. Those coordinates are the triple-point coordinates provided they do not belong to the reflecting surface. The resulting shock positions are superimposed onto the pressure color map in Fig. 7C. It is made clear that the case $(8 \cdot 10^{-3},\ 3.5°)$ corresponds to an IR.

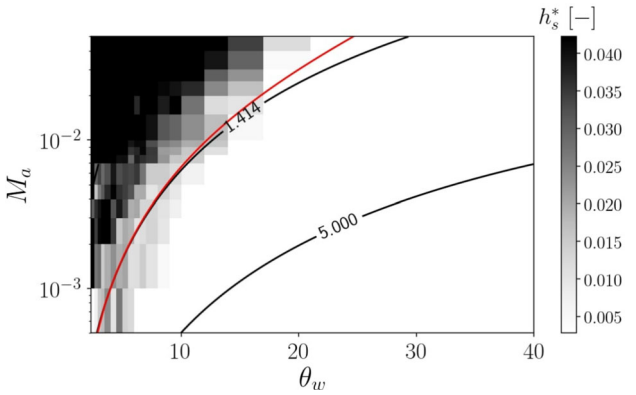

Fig. 8 Color map of a Mach stem height h_s resulting from reflection cases of a step shock obtained with the detection algorithm presented in Sect. 3.3 along with the iso-contour for certain values of a (black lines) and the value of a_D (red line)

The obtained results following such algorithm are presented in Fig. 8 where the normalized height of the Mach stem $h_s^* = h_s/(c_0 \cdot t_{ref})$—with h_s the absolute Mach stem height measured at the instant t_{ref}—is displayed for every investigated couple $(\theta_w,\ M_a)$, representing a total of 368 combinations. The $a_c = \sqrt{2}$ limit is displayed in Fig. 8. On the same figure, in red is the a_D parameter calculated with the theoretical detachment condition as introduced in Sect. 3.1.1.

The size of the Mach stem increases as expected for low angles and higher Mach numbers as the reflection pattern is already known to go from RR to NLRR to IR with the decrease of θ_w for a given Mach number. Additionally, despite the δ increment being set to $\Delta\delta = 2°$, the Mach stem position is accurately depicted. The threshold of $a_c = \sqrt{2}$ serves as a clear separation, distinguishing regions with the presence of a triple point (indicated in black) from those without it (indicated in white). Moreover, a_D (red line) is better than $a = \sqrt{2}$, especially at high M_a as expected. It seems that for low Mach number and low wedge angle, the Mach stem is detected slightly prematurely, meaning on the right side of the curve $a_c = \sqrt{2}$. The main reason is that the acoustic Mach numbers in that region are very weak, making shock detection less accurate compared to stronger shocks. This affects the precision of the triple-point position, which is determined based on the incident and reflected shock detection.

In their paper, Desjouy et al. [27] also reported results on the position of the Mach stem, but these were based on a cylindrical propagating N-wave. Their results do not show the premature detection of the Mach stem, which could be due to two reasons: either the color scale he used does not allow this feature to be seen, or, more likely, the behavior of the N-wave differs from that of the step shock. Desjouy et al.'s findings with cylindrical N-waves [27] indicate that variations in the angle have a stronger influence on the value

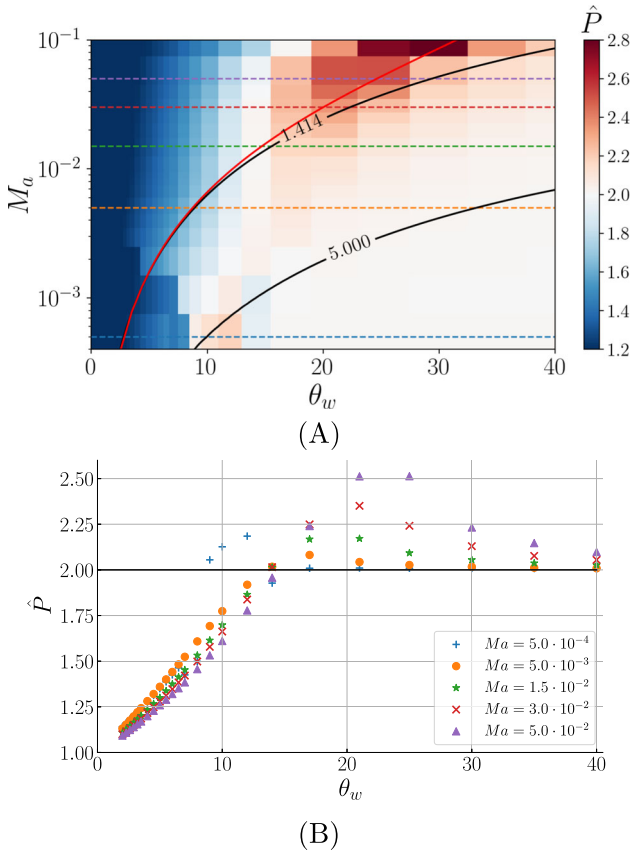

Fig. 9 **A** Color map of the value of $\hat{P}$ behind the reflected shock for the step shock database along with the theoretical limit values of a for the reflection transition (black lines) and the detachment condition (red line) $\delta = 0°$; **B** Iso-Mach value of $\hat{P}$ for different M_a values

of h_s, which contrasts with our observations. In our case, both the acoustic Mach number and the wedge angle seem to affect the size of the Mach stem, highlighting the difference between cylindrical and plane N-wave behaviors.

3.4 Sole signal analysis

The value of $\hat{P}$ behind the incident shock is $\hat{P} = 1$, since it is normalized by the pressure jump downstream of a normal shock with the same amplitude. However, behind the reflected shock $\hat{P}$ can take different values. For example, in the case of a regular linear reflection, its value equals 2 as verified by the Rankine–Hugoniot equations. The color map presented in Fig. 9A has been constructed based on the data collected from a specific numerical probe positioned within the domain as shown in Fig. 1. In Fig. 9A, $\delta = 0°$, corresponding to a probe located on the reflecting surface. The probe position $x_p = 0.6$ m is taken sufficiently far from the wedge to visualize the Mach stem. The color map illustrates the maximum value behind the reflected shock $\hat{P}$ for each couple $(\theta_w,\ M_a)$.

Black lines in Fig. 9A represent the limits based on the parameter a whereas the red line is the theoretical detachment criterion (see (6)). We can observe that any $(\theta_w,\ M_a)$ couple leading to values of a above 5 respects the criteria as their color is close to the white shade representing the theoretical value of $\hat{P} = 2$. In the same region, the slight tendency for extremely low M_a to reach values of $\hat{P}$ above 2 is due to oscillations of the solution that peaks at a maximum higher than $\hat{P} = 2$. At other positions, any difference from that theoretical value of linear reflection ($\hat{P} = 2$) is proof of the nonlinear behavior for the reflected shock.

It can be observed that for the different Mach values across the M_a region, the pressure $\hat{P}$ effectively goes through a maximum above 2 as predicted in the literature [31]. This behavior confirms the relevance of the results presented in Fig. 9.

Also, the numerical study performed by Sparrow and Raspet [31] (also visible in Baskar et al. [10]) proved that close to the transition region, the pressure $\hat{P}$ should peak above 2 before returning to 2 for very low angle values. To validate this behavior, the study of different iso-Mach lines in the domain is performed for multiple acoustic Mach number values and plotted in Fig. 9B. For each case, there is a maximum value of $\hat{P}$ above 2. A noticeable difference can be observed between the maximum value of the work of Baskar et al. [10], and the present work. While Baskar et al. [10] find a maximum around 3.5, this work finds a maximum about 2.5, similar to the value found in Sparrow and Raspet [31]. Each M_a value seems to behave similarly except for the weakest acoustic Mach $M_a = 5 \cdot 10^{-4}$ where the gap between values below 2 and above 2 is quite sharp. This might be due to small oscillations that have already been observed for the simulation of a very low value of acoustic Mach number. Also, the higher the acoustic Mach number, the higher the overshoot above 2.

4 Extension to N-waves

In the previous section, our focus was primarily on the study of step shock reflections and their associated transition limits. In this section, we shift the analysis to a different type of wave known as an N-wave. This wave, which closely resembles real-life signals, has a distinctive pattern: it begins with a sharp pressure front, followed by a linear pressure decrease. This progression eventually results in a sharp rear shock, which brings the pressure back to its initial value. The computational domain remains consistent with the one employed in the step shock study. The demonstration found in Appendix 2 establishes that the pressure decay resulting from the nonlinear contribution is of the same order of magnitude as the geometric pressure decay. This result validates the 2D planar wave as a framework for analyzing nonlinear effects.

4.1 N-wave acoustic range

From experimental measurements [32] and ballistic assumptions, we were able to set a range in amplitude that fits with the characteristic amplitude levels a microphone could experience in an urban environment for the detection of acoustical shock waves. The maximum acoustic pressures have been measured around 7000 Pa from the muzzle blast for a distance of 1 m of an AK-47 [32]. For the Mach wave of a bullet shot from an AK-47 from a 300-m shot distance and a miss distance of 25 m, the measurement is around 100 Pa in amplitude [19]. Regarding those experimental values, the range for our N-wave numerical study has been set to 50 Pa $< p_{\max} <$ 8000 Pa with $p_{\max}$ the peak pressure of the N-wave leading shock front. The initiation of the N-wave within the domain involves configuring the waveform to resemble an N-shape through a function constructed with two discontinuities connected by a linear pressure decrease at a specific interval corresponding to $\lambda_N = 0.1$m, the signal wavelength, kept constant in this study. The N-wave rear shock is positioned initially at $x_0 = x_c - 0.2$(m). Subsequently, the state variables are initialized to ensure the signal propagates toward the wedge while satisfying the unsteady Riemann invariants. The different flow quantities (P, u, T) at initialization are given below. The N-wave form is defined using both the pressure and an analytical function g_N that generates the characteristic N-shape with a wavelength λ_N:

$$g_N = P_0 \left(\frac{2}{\lambda_N} |x - \lambda_N \lfloor \frac{x}{\lambda_N} + 0.00001 \rfloor| - 1 \right) \tag{10}$$

Thus, the pressure is expressed as:

$$P(x) = \begin{cases} P_0 & \text{if } x < x_0, \\ P_0 & \text{if } x > x_0 + \lambda_N, \\ P_0 + \mathrm{d}P & \text{otherwise, } \mathrm{d}P = g_N \cdot M_a \cdot \gamma \end{cases} \tag{11}$$

The expression for the velocity is as follows:

$$u(x) = \begin{cases} u_0 & \text{if } x < x_0, \\ u_0 & \text{if } x > x_0 + \lambda_N, \\ u_0 + \mathrm{d}u & \text{otherwise} \\ & \text{with } \mathrm{d}u = \frac{2c_0}{\gamma - 1} \left(\left(\frac{P}{P_0} \right)^{\frac{2\gamma}{\gamma - 1}} - 1 \right) \end{cases} \tag{12}$$

Since the N-wave propagates uni-directionally, the components of velocity in all other directions are zero. Finally, the temperature verifies:

$$T(x) = \begin{cases} T_0 & \text{if } x < x_0, \\ T_0 & \text{if } x > x_0 + \lambda_N, \\ T_0 \left(\frac{P_0 + \mathrm{d}P}{P_0} \right)^{\frac{\gamma - 1}{\gamma}} & \text{otherwise.} \end{cases} \tag{13}$$

The demonstration of the initialization may be found in Appendix 3.

4.2 Front and rear shock triple-point detection

The self-similarity of the propagation and reflection of a step shock is inherent in its construction in an inviscid fluid described by the Euler equations used in this study. This contrasts significantly with N-waves, where the N-shape compels the signal to spread, leading to a consistent alteration of state variables during both propagation and interaction. Consequently, this breaks the observed self-similarity characteristic of the step shock configuration.

The evolution of the Mach stem height is investigated in this section, based on the algorithm given in the previous section 3.3. Two different simulation results are presented in Fig. 10 where the pressure distribution of a reflecting N-wave can be observed. The point of intersection of the incident and reflected leading shock in Fig. 10A seems to belong to the surface. Additionally, the reflected leading shock exhibits a curved shape from the point of reflection. These combined observations suggest a nonlinear regular reflection (NLRR) scenario. The specific (θ_w, M_a) combination in Fig. 10A corresponds to a value of a equal to 1.035 for the leading shock. However, it is noteworthy that a values below $a_c = \sqrt{2}$ should typically lead to an irregular reflection (IR) in the case of step shocks, which is not obvious here. This observed discrepancy is expected due to the fundamental waveform differences between step shocks and N-waves. Furthermore, Fig. 10B illustrates an IR scenario, where the point of intersection between the leading incident and reflected shocks is detached from the wedge's surface, with a corresponding a value of 0.672. This suggests that the transition threshold between regular and irregular reflection appears to be lower for N-waves compared to step shocks. This behavior is backed up by Baskar et al.'s numerical analysis [10] as well as Karzova et al's. experimental study [26], both of which suggested a lower a value for the transition from regular to irregular reflection. However, it is important to note that these studies did not converge toward the same threshold value. While Baskar et al. assumed a transition around $a = 0.8$, Karzova et al's. experimental studies suggested a slightly higher value of $a = 1.05$. One potential explanation for this discrepancy is that Karzova et al. examined cylindrical N-waves, whereas Baskar et al. considered planar N-waves, consistent with the approach in our study. Therefore, our

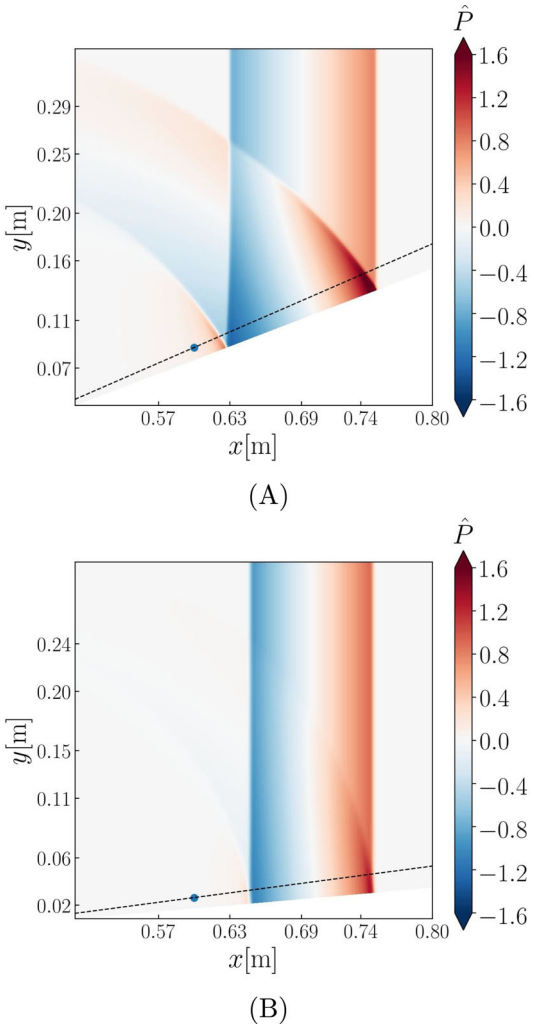

Fig. 10 Simulation results for the propagation of an N-wave onto a wedge of angle **A** $\theta_w = 21°$ and **B** $\theta_w = 5°$ for an acoustic Mach number $M_a = 5 \cdot 10^{-2}$ and $M_a = 7 \cdot 10^{-3}$, respectively

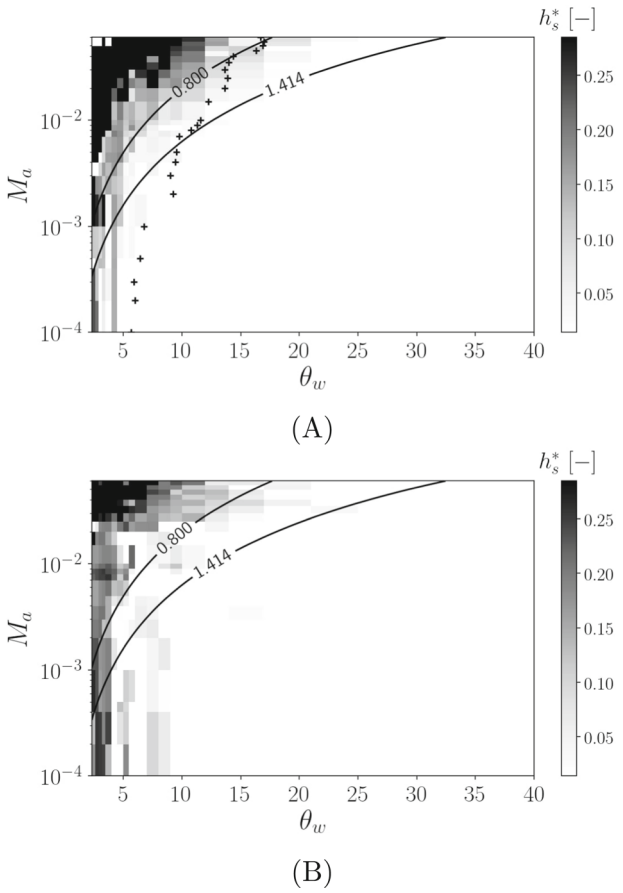

Fig. 11 Color map of a Mach stem height h_s resulting from reflection cases of an N-wave, obtained similarly as Fig. 8 with a modified algorithm for the N-wave: **A** the leading shock of the N-wave and **B** the rear shock. Black lines represent iso-contour for certain values of a. Crosses in (**A**) represent θ_{lim} values discussed in 4.3.1

transition should match with Baskar et al's. transition limits for each specific case rather than only the two particular cases presented in Fig. 10.

To verify so, the same treatment as the one performed on the step shock pressure field is applied here to retrieve the Mach stem height. Some changes were made in the algorithm, especially the distinction between the negative and the positive part of the N-wave in order to study the leading shock and the rear shock separately. The color maps of the Mach stem heights are thus obtained in Fig. 11.

Figure 11A depicts the leading shock Mach stem height evaluated with the Mach stem detection algorithm on the whole (θ_w, M_a) domain along with both approximated limits $a = 0.8$ from Baskar et al. [10] and $a_c = \sqrt{2}$ that can be found in solid lines. In regions where the map appears white, it signifies that no Mach stem has been detected, indicating regular reflection. Conversely, the presence of a Mach stem is indicated by any gray shading, with the size of the Mach stem increasing as the shading becomes darker. As the reflected shock experiences a favorable pressure gradient, it is less "constrained" than when it develops downstream of a step shock. Consequently, it is expected that the values of h_s will be higher in this scenario compared to the case of a step shock, which is indeed observed.

The expected shift of the transition limit toward $a = 0.8$ is not verified here. Although there is a noticeable change in the limit compared to the case of a step shock, it is not substantial enough to clearly establish the transition limit at $a = 0.8$. One possible explanation for this modest difference might be associated with the loss of self-similarity for the reflection of an N-wave, in contrast to the reflection of a step shock. Consequently, as the leading shock propagates, the pressure decreases with distance as $\mathcal{O}\left(1/\sqrt{x}\right)$ (see (25)), increasing the value of a, and ultimately leading to a RR for all cases. In our case, it is possible that the instant from which the pressure field is extracted does not correspond to a similar instant as the one presented in Baskar et al.'s analysis,

hence the noticeable difference in the transition limit for the reflection of the shock front.

In Fig. 11B, the rear shock reflection transition limit appears to be smaller than the one for the shock front. For a similar case, the Mach stem height is less for the rear shock than for the front.

4.3 Energy spectral density analysis

The interest of spectral analysis is its direct application to a time signal typically recorded from a microphone. In the specific context of this paper, which focuses on enhancing source localization, this is a valuable analysis since pressure signals are usually recorded using those types of devices.

4.3.1 Empirical study

The signature of $\hat{P}$ is studied in the frequency domain using the one-sided energy spectral density (ESD). Here, energy refers to the generalized sense of signal processing energy represented by the integral of the square of the time signal, which is expressed in the frequency domain using the fast Fourier transform (FFT):

$$\mathcal{E}_{\hat{P}} = 2\left|\int_{-\infty}^{+\infty} \mathrm{e}^{-i2\pi ft}\hat{P}(t)\mathrm{d}t\right|^2, \quad f \in \mathbb{R}^+ \tag{14}$$

Here, we will use a log scale of the normalized signal as follows:

$$\mathcal{E}_{\hat{P}}^{\mathrm{dB}} = 20\log\left(\frac{\mathcal{E}_{\hat{P}}}{\max\left(\mathcal{E}_{\hat{P}}\right)}\right) \tag{15}$$

The energy spectral density is used in Sabatini et al. [33] in the context of infra-sound atmospheric propagation to specify the frequency bandwidth associated with the main contribution of the received signal. Similarly, the ESD is treated here to understand which part of the spectrum could be associated with nonlinearities.

Figure 12 is obtained by taking the ESD of each recorded signal of an N-wave reflection onto different wedge angles and plotting it against that very same value of θ_{w} for a given Mach number. Recordings are obtained for a given probe location chosen to be close enough to capture the essential information related to N-wave reflection: $\delta = 2.55°$ and $x_{\mathrm{probe}} = 0.6$ m. Results are presented with a frequency f^* normalized with the frequency $f_{\mathrm{N},0}$ of the N-wave at time $t = 0$:

$$f^* = \frac{f}{f_{\mathrm{N},0}} \quad \text{with} \quad f_{\mathrm{N},0} = \frac{c_0}{\lambda_{\mathrm{N}}(t=0)} \tag{16}$$

where $\lambda_{\mathrm{N}}(t = 0)$ is the wavelength of the N-wave at $t = 0$.

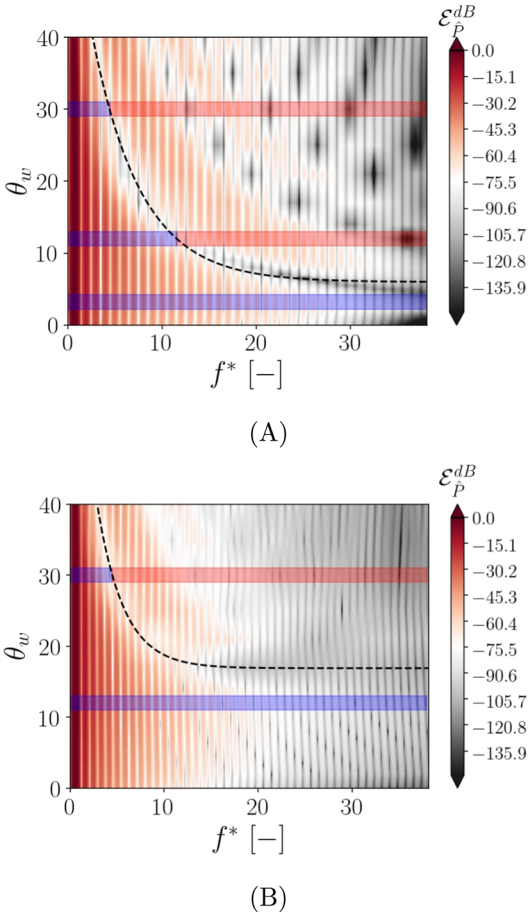

Fig. 12 Color map of energy spectral density as a function of the wedge angle θ_{w} for **A** $M_{\mathrm{a}} = 5 \cdot 10^{-2}$ and **B** $M_{\mathrm{a}} = 2 \cdot 10^{-4}$ for a probe location $\delta = 2.55°$ and $x_{\mathrm{probe}} = 0.6$ m

When observing Fig. 12, and for a given M_{a}, it seems that, as θ_{w} decreases, the first lowest energetic point of the ESD shifts toward higher frequencies to end up with an asymptotic value. The evolution appears to follow an exponential trend of the form:

$$\theta(f) = m\mathrm{e}^{-tf} + \theta_{\mathrm{lim}} \tag{17}$$

with the coefficients $(m,\ t,\ \theta_{\mathrm{lim}})$, approximated from the interpolation of the hand-picked values of the low energy zone (white area), separating the spectrum in two main regions. Parameters $(m, t, \theta_{\mathrm{lim}})$ are determined for each different Mach number though Fig. 12 only provides the extreme cases in terms of M_{a} that are $M_{\mathrm{a}} = 2 \cdot 10^{-4}$ and $M_{\mathrm{a}} = 5 \cdot 10^{-2}$. The resulting exponential function $\theta(f)$ is plotted back on the ESD field with the visible black dashed line. This function indicates that for every value of θ_{w}, there is a corresponding frequency f that divides the spectrum into two distinct regions up until the asymptotic value θ_{lim} is reached. Examples of such a spectrum decomposition are given in Fig. 12A represented by various colors: The

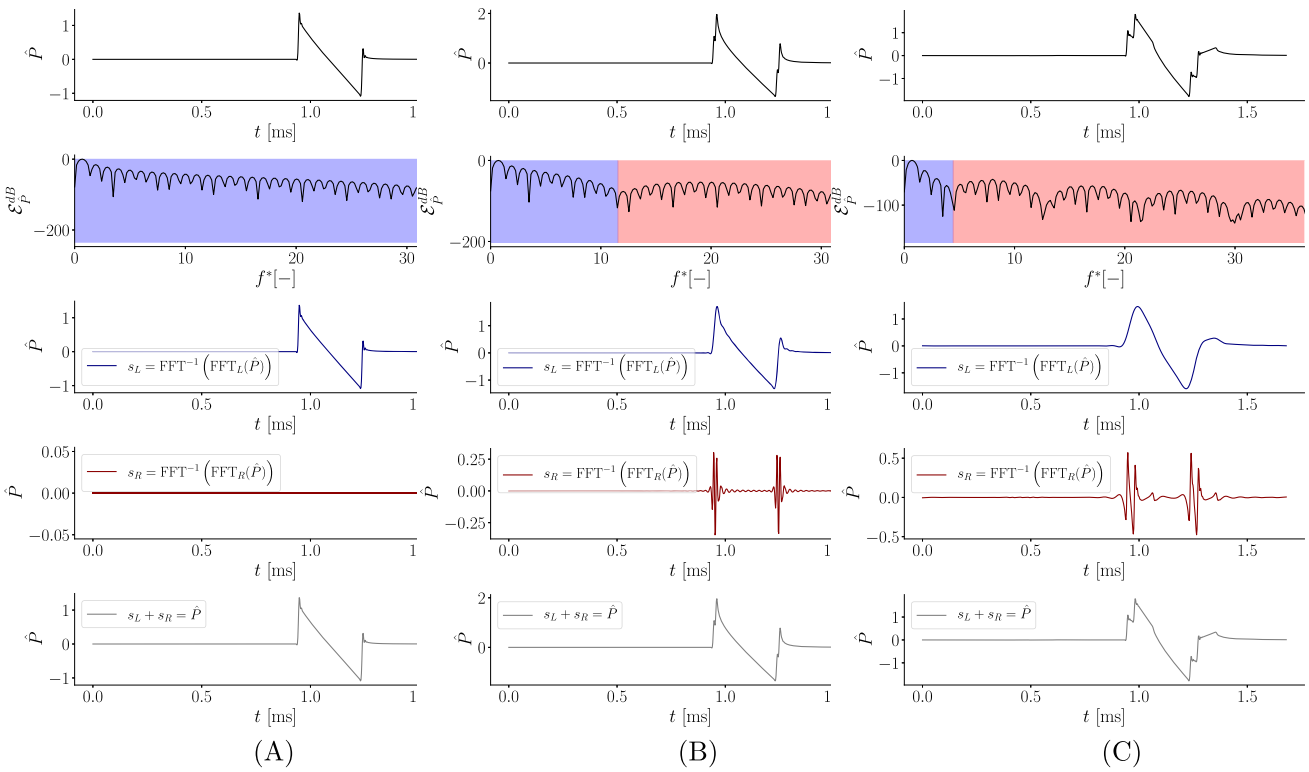

Fig. 13 Pressure time-signal reconstruction from inverse FFT for the same $M_a = 2 \cdot 10^{-4}$ taken from Fig 12A: **A** $\theta_w = 3.2°$, **B** $\theta_w = 12°$, and **C** $\theta_w = 30°$. From top to bottom: raw signal; highlighted left and right regions from FFT; signal reconstructed from left region of the FFT; signal reconstructed from right region of the FFT; summation of left and right reconstructed signal

light blue shading represents the frequency bandwidth that remains to the left of $\theta(f)$ and the light red shading denotes the frequency bandwidth to its right. Such a decomposition was performed for three wedge angle values $\theta_w = 30°$, $\theta_w = 12°$, and $\theta_w = 3.2°$ represented with the three horizontal colored bands in Fig. 12A. The bandwidth of the case $\theta_w = 3.2°$ remains light blue and is not divided into two regions because its value remains below the θ_{lim} value: $3.2° < \theta_{lim} = 7°$ in this case.

Figure 13A provides a comparison of the different contributions of the two spectrum regions (light blue and light red) in the generation of the entire recorded acoustic pressure signal. To achieve this, the fast Fourier transform (FFT) of the signal is employed instead of the energy spectral density (ESD). This choice is made because, during the construction of the ESD, certain information, particularly the phase of the signal, becomes inaccessible, making it impossible to reconstruct the equivalent time signal through an inverse FFT.

To recreate the time pressure signal (top curve of Fig. 13) representative of a specified frequency bandwidth, we had to perform the inverse Fourier transform onto the FFT that was initially filtered with this specified bandwidth. More specifically, the applied filtering consists of putting zero for each Fourier coefficient outside of the specified frequency range. Afterward, when concatenating both recreated signals, the original signal should be retrieved.

The results provided in Fig. 13 were obtained through the use of this treatment. As observed, it gives the recreated time signal s_L (in blue) by only taking into account the spectrum on the left side of the valley of low energy described above (third curve from the top). On the other hand, the fourth curve represents the equivalent time signal s_R (in red) recreated only from the consideration of the region located on the right part of the low energy zone. We define both reconstructed signals as

$$s_{L/R} = \mathrm{FFT}^{-1}\left(\mathrm{FFT}_{L/R}(\hat{P})\right) \tag{18}$$

with FFT_L and FFT_R the filtered FFT from the frequency range left side of f and right side of it, respectively. Finally, the summation of both parts recreates the exact same signal (gray in the last curve of Fig. 13) as the recorded one (black in the first curve of Fig. 13) and no information was lost in the process. This result is expected as the FFT is bijective but it is presented here as a validation of the different frequency contributions. The same treatment is applied for other (θ_w, M_a) couples not shown here.

The right part of the signal appears to contain critical information about the shocks, including both the incident and reflected components. Specifically, when comparing signals at different angles, s_R seems to be the signal where the reflection is most "visible", characterized by two peaks on each front (as seen in the top curves of Fig. 13B and C), in contrast to signals with only one peak (such as the top curve of Fig. 13A). The specific case in Fig. 13B supports this observation, as the two peaks—though still visible—are closer together, resulting in a reconstructed s_R of lower amplitude compared to the other cases presented. A signal with only one peak may either be from a probe placed too close to the reflecting surface to differentiate between the reflected and incident shocks, or it may correspond to a single wave, suggesting the presence of a Mach stem. Discontinuities have high-frequency terms within their spectral decomposition. Therefore, the high-frequency content of the signal, which corresponds to this right portion of the spectrum, contains information about both shocks and offers insight into the reflection. However, it is important to note that the reflection cannot be fully identified by examining the high-frequency part alone.

The full-time signal was retained due to the "natural" zero-padding effect, which occurs as the probe waits for the signal to pass. The decision to discard the option of studying a truncated signal was made to exploit the benefits of zero-padding. Specifically, zero-padding not only increases the length of the signal, improving frequency resolution, but it also introduces a synthetic low-frequency component in the initial segment of the FFT. This helps reduce spectral leakage by making the non-periodic signal appears more periodic, thereby confining energy to narrower frequency bands. Additionally, it enhances the ability to distinguish between the frequencies related to the zero-padding and those corresponding to the actual recorded signal, resulting in a smoother Fourier spectrum that better isolates and identifies the true frequencies of interest.

The expression of $\theta(f) = me^{-tf} + \theta_{\text{lim}}$ is characterized with an asymptotic value of wedge angle $\theta_w = \theta_{\text{lim}}$. This specific value is different for each of the plotted cases in Fig. 12: it increases with the acoustical Mach number M_a. Thus, there is a couple $(\theta_{\text{lim}}, M_a)$ corresponding to the asymptotic value of θ_w for a given acoustic Mach number. The obtained couples $(\theta_{\text{lim}}, M_a)$ are plotted on top of the normalized Mach stem height h_s^* color map in Fig. 11A, the separation between the presence and the absence of a Mach stem seems to fit with this asymptotic limit:

— below the limit, $h_s^* \approx 0$ indicates a RR;

— above the limit, $h_s^* > 0$ indicates an IR.

Therefore, by searching for the existence of the first inflection point in the ESD, it is possible to identify two regions of the spectra, allowing to assert the existence of a regular reflection (RR). Whenever the inflection point is not retrieved, the irregular reflection (IR) is a possibility. From these results, we can deduce that the spectral analysis can differentiate RR from IR based on the analysis of a single probe in time.

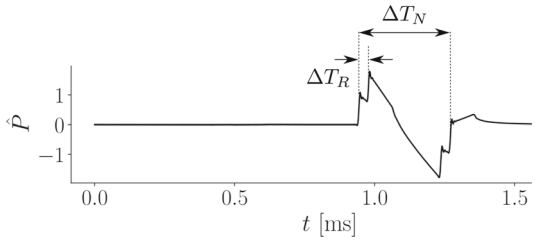

Fig. 14 Visualization for the time interval ΔT_R and ΔT_N

4.3.2 Analytical study

To understand where the low energy zone is coming from, the time interval between each front (incident/reflected or front/rear as illustrated in Fig. 14) has been measured thanks to a feature developed in the Mach stem detection algorithm. In Fig. 14, the different time intervals ΔT_R and ΔT_N are represented with ΔT_R the time difference between incident and reflected shock of the front shock and ΔT_N the period of the N-wave at the point of measurement.

In Fig. 15, the time intervals associated frequencies are drawn on top of the ESD cartography for $M_a = 2 \cdot 10^{-4}$. Blue dots represent the values for $1/\Delta T_R$, while the red dots (on the left) represent the values for $1/\Delta T_N$. As expected, the red dots are the same for each different angle as they correspond to the N-wave period that remains the same for each angle. The blue dots follow the second most energetic frequency that we can therefore associate with the incident and reflected shock delay. Whenever blue dots have a zero value in frequency (left of Fig. 15), it means that the algorithm did not detect two distinct peaks which should be a sign of a Mach stem reflection happening. It is possible to determine at which angle it happens by visualizing the angle between the last blue point on the map and the first blue point on zero. For instance, in Fig. 15, the detachment seems to happen between $\theta_{\text{lim}} = 10°$ and $\theta_{\text{lim}} = 12°$. These values, if compared with the asymptotic value of the same case Fig. 12 are over-evaluated.

The black crosses represent the mean value between a red dot and a blue dot. It appears that the black crosses follow the low-density valley identified with the spectral analysis. It is therefore possible to get an analytical expression for this low energy zone which is defined as follows:

$$f = \frac{1/\Delta T_R + 1/\Delta T_N}{2}. \tag{19}$$

Note that both a blue point and a black cross seem out of validity, this is due to an algorithm detection failure.

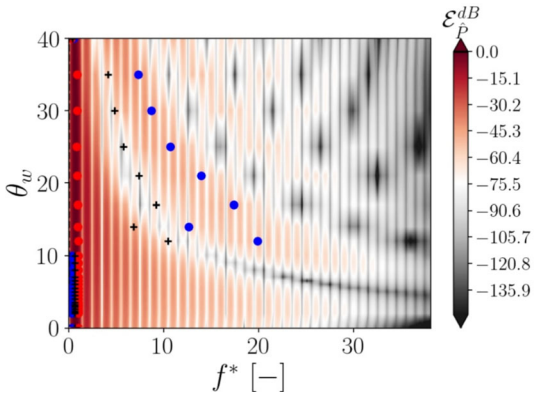

Fig. 15 Evaluated time interval between the incident and reflected shock of the front shock (blue), the time interval of the full N-wave (red), and the average of both (black crosses) on top of the color map provided in Fig. 12A

5 Conclusions

The determination of markers of nonlinearity in the interaction of an acoustical shock is a demanding process. The simulations performed in this paper did not account for many real-life physical constraints such as complex geometries, potential wind, or 3D effects. However, the provided work singled out two methods capable of distinguishing irregular reflection—potentially a source of uncertainties regarding the localization process—in restrictive planar 2D cases. The first method would be based on the analysis of the ESD and the search for an inflection point. A simpler second method showed good agreement between the analytical expression and the "low energy" zone in the ESD, corresponding to its first inflection point. This thorough study of simple waveforms is an invitation to increase the complexity. In the following, different points sum up the observed conclusion.

The first part of this paper focused on reflections on a step shock. It provided a comparison with the literature for three given cases and asserted that the general behavior is well retrieved, especially regarding the obtained reflection types. A large range of simulations was performed on the control parameter couple (θ_w, M_a), namely the angle of the corner and the acoustic Mach number.

The critical value of $a_c = \sqrt{2}$ used to assess the transition between NLRR and IR was compared with the detachment condition expressed by Mouton and Hornung's formulation [30]. It has been seen that the parameter a provided a good estimation of the prediction of an IR for grazing angles. However, on the overall spectra of the performed cases, the detachment condition applied to the calculation of a_D is still a better option, as it provides an estimation of the transition not only for grazing angles but for all wedge angles. This parameter has been adapted from Mouton's work [29] to fit with the unsteady acoustical shock formalism. In this work, it is referenced as $a_D = f(\theta_{w,D})$.

Then, the reflection of N-waves has been studied over a range of 50 Pa $< p_a <$ 8000 Pa in amplitude and $0° < \theta_w < 40°$ in wedge angle. It has been observed from a Mach stem detection analysis that the transition limit occurs for lower parameter a value than for a step shock. However, the value $a = 0.8$ found by Baskar et al. [10] was not retrieved here. The transition seems to happen between $a = \sqrt{2}$ and $a = 0.8$. The Mach stem detection performed on the rear shock revealed a value in the transition even smaller than the one found for the leading shock. This is the first time such an analysis has been performed on the rear shock of an N-wave.

The analysis of the energy spectral density enabled the separation between two distinctive parts of the spectra: one containing the reflection information, and the other one containing the rest of the acoustic signal information. In addition, asymptotic behavior was observed in terms of the low energetic valley used to divide the spectra in the first place. In fact, the trend of this valley followed an exponential law, ending in an asymptotic value that represents the limit in θ_w where the distinction between the reflection of the signal and the rest of the signal was no longer feasible. Since the absence of reflection in the signal has already been interpreted as a signal taken too far from the surface, or a signal incorporating a Mach stem, a link has been made with the Mach stem height color map of the leading shock. The results presented in Fig. 11A provided the conclusion that any reflecting condition ensuring (θ_w, M_a) to be above the limit would indicate a RR; while any (θ_w, M_a) below that limit would indicate an IR. Therefore, in the source localization context, the spectral analysis near the wall surface may prove to be quite useful to indicate an IR based on time pressure profiles.

Appendix 1: Grid convergence study

In order to assess the grid efficiency in our simulation results, the Richardson method [34] is used to retrieve the apparent convergence p_{app} of the numerical scheme used in the calculation.

It is possible to retrieve the error as a function of the grid size (see Fig. 16B). Three grid levels $i = [h/2, h, 2h]$ have been chosen to be in the asymptotic range of convergence as the numerical error is following the law

$$\varepsilon = \alpha h^{p_{app}} \tag{20}$$

where h is the grid size and α is a constant. The characteristics of the three meshes used are given in Table 2.

Here, the acoustical signal energy E_{ac}^{j} is used as a convergence criterion. We define, for each grid $j = [h/2, h, 2h]$,

Table 2 Grid convergence analysis

Name	N_{cells}	$h = N_{\text{cells}}^{-1/2}\,[\text{m}^{-1}]$	$\frac{h}{h_{\text{ref}}}$
$h/2$	0.13 M	$2.77 \cdot 10^{-3}$	0.5
h	0.52 M	$1.39 \cdot 10^{-3}$	1.0
$2\,h$	2.08 M	$6.9 \cdot 10^{-4}$	2.0

E_{ac}^{j} as follows:

$$E_{\text{ac}}^{j} = \sum_{i=1}^{N} \int_{-\infty}^{+\infty} \hat{P}_i^2(x)\mathrm{d}x \tag{21}$$

that represents the sum of different instants of the integral of the acoustic signal energy. Here, six instants were taken for the computation which gives $N = 6$. The estimation of this criterion at constant CFL enables to take into account both the effect of time and space discretization of the solution.

The Richardson extrapolated value of the quantity studied $\phi_i = E_{\text{ac}}^{i}$ is given by

$$\phi_{\text{RE}} = \frac{r_{h,h/2}^{p_{\text{app}}}\phi_{h/2} - \phi_h}{r_{h,h/2}^{p_{\text{app}}} - 1} \tag{22}$$

and the relative error of ϕ computed with different grid levels is expressed as

$$\varepsilon_i^* = \left| \frac{\phi_{\text{RE}} - \phi_i}{\phi_{\text{RE}}} \right| \tag{23}$$

The apparent order of convergence p_{app} is defined as

$$p_{\text{app}} = \frac{\ln\left|\varepsilon_{2h,h}/\varepsilon_{h,h/2}\right|}{\ln(r_{h,h/2})} \tag{24}$$

with $\varepsilon_{i,j} = \phi_i - \phi_j$ and the grid refinement coefficient $r_{i,j} = \frac{h_i}{h_j} = 2$.

Finally, the evaluation is performed in the case where $(\theta_{\text{w}}, M_{\text{a}}) = (10°, 3.10^{-2})$. The order of convergence, p_{app}, defined in (24) takes the value of 4.512, which is above the theoretical order of convergence 3 for the spectral scheme used. This order of convergence visible in Fig. 16 provides a very good conclusion on the refinement of the mesh used for the simulation performed in this manuscript.

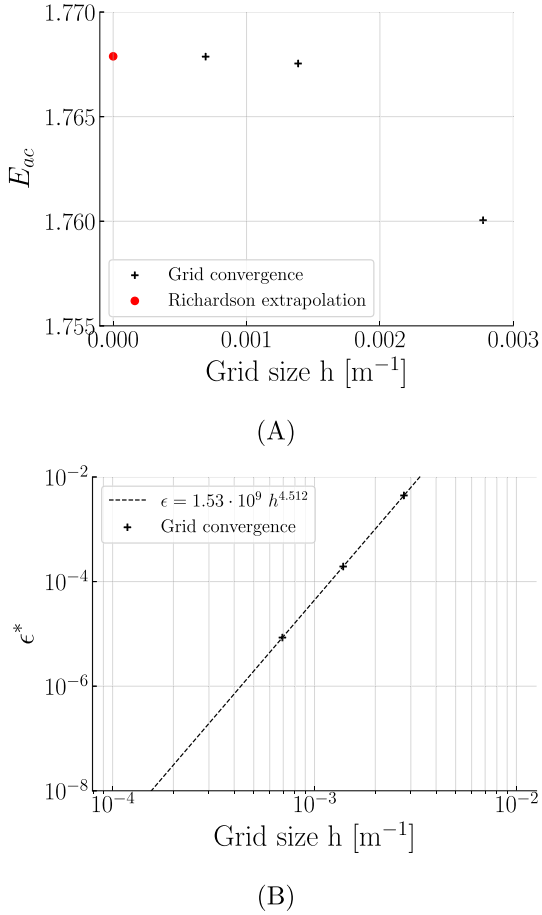

Fig. 16 Mesh convergence study using Richardson extrapolation: **A** grid size influence on the value of E_{ac} and **B** the relative error as a function of the grid size

Appendix 2: Coupling nonlinear and cylindrical decays

The aim of this section is to propose a method to couple the well-known cylindrical decay of linear acoustic waves to the planar nonlinear decay of the amplitude of N-waves, due to shock/expansion interaction.

Two parameters characterize an N-wave: its wavelength λ and its amplitude M_{a} or the acoustic pressure p_{a}. The evolution of the pressure p_{a} and the wavelength λ of the N-wave can be described as [35]:

$$p_{\text{a}}(x) = \frac{p_{\text{a},0}}{A(x_0, x)} \tag{25}$$

$$\lambda(x) = \lambda_0\, A(x_0, x) \tag{26}$$

where $A(x_0, x) = \sqrt{1 + \frac{\gamma+1}{\gamma}\frac{x-x_0}{\lambda(x_0)}\frac{p_{\text{a}}(x_0)}{P_0}}$, so that $p_{\text{a}}(x)\lambda(x)$ is ensured to be kept constant, with $p_{\text{a}}(x_0)$ being the acoustic over-pressure at initialization and P_0 being the ambient pressure which ratio quantify the nonlinear effect.

Similarly, the well-known pressure decrease of a 2D cylindrical wave is given by $p_{\text{cyl}(r)} = p_{\text{a},0}\sqrt{\frac{R_0}{r}}$.

To combine both effects, the pressure amplitude laws are rewritten as differential equations in order to identify the change rate. Both change rates are then added to provide a

law for the evolution of a cylindrical N-wave. The integration of such an equation is given by

$$p_{\mathrm{a},i} = p_{\mathrm{a},i-1} + \delta p_{\mathrm{a}}^{\mathrm{cyl}} + \delta p_{\mathrm{a}}^{\mathrm{NL}} \tag{27}$$

where $p_{\mathrm{a},i} = p_{\mathrm{a}}(r_i)$ are the successive wave amplitudes along r_i.

The differential law that ensures the decay of a linear cylindrical acoustic wave p_{cyl} can be written as:

$$\delta p_{\mathrm{a}}^{\mathrm{cyl}} = -\frac{1}{2}\frac{p_{\mathrm{a},i}}{r_i}\delta r \tag{28}$$

The evolution of $\delta p_{\mathrm{a}}^{\mathrm{NL}}$ is given by

$$\delta p_{\mathrm{a}}^{\mathrm{NL}} = p_{\mathrm{a},i} - p_{\mathrm{a},i-1} = p_{\mathrm{a},i-1}\left(\frac{1}{A_{i-1}} - 1\right) \tag{29}$$

as, according to (25), a direct evolution from r_{i-1} to r_i where $x_0 = r_{\mathrm{i}-1}$ and $x = r_i$ (instead of an actual differentiation). This step needs to additionally integrate $\lambda(r)$ with $\lambda_i = \lambda_{i-1} A_{r_{i-1},r_i}$. This pressure evolution of a cylindrical N-wave then combines both geometrical pressure decay and N-shaped-related pressure decay.

A series of simulations regarding the propagation of cylindrical N-waves have been performed, and specifics can be found in Deleu's work [36].

Figure 17 gives a comparison of the simulation results with theoretical results. The decay is plotted against normalized $\lambda^* = \lambda/\lambda_{\mathrm{N}}$. The crosses represent the different pressure amplitudes measured by numerical probes for three different simulation cases. The theoretical integrated expressions for the pressure decay (25) (wavelength spreading (26) is not illustrated here) are for both plane and cylindrical N-wave.

From the analytical expression of each nonlinear contribution (Eqs. (25)–(26)), the computation of the cumulative effect of both geometrical and nonlinear features is performed and referenced in Fig. 17 (solid line). The dashed line gives a sense of the pressure decrease of a simple plane N-wave. When combining both effects, the decrease is all the more important. Here, different strength values are presented: $M_{\mathrm{a}} = 9.4 \cdot 10^{-2}$ (black), $M_{\mathrm{a}} = 4.7 \cdot 10^{-2}$ (blue), and $M_{\mathrm{a}} = 10^{-3}$ (red).

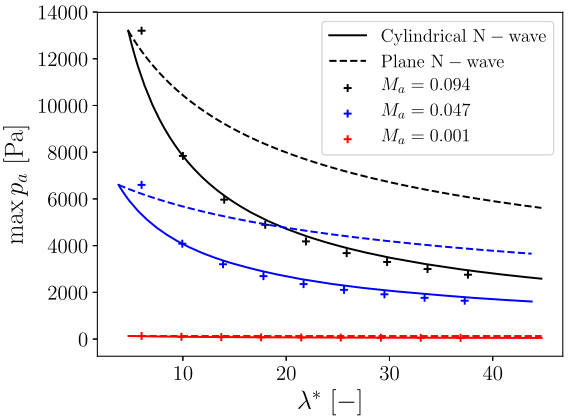

Fig. 17 Over-pressure p_{a} between cylindrical N-wave (solid line) and plane N-wave (dashed line) propagation nonlinearities for several initial M_{a}

Appendix 3: Initialization of the waveform

In the case of plane N-waves, the amplitude (acoustic Mach number M_{a}) and the Riemann invariants were considered as input parameters. This appendix details how the plane N-wave was initialized.

It is important to note that the same method is used for initializing step shocks, but in this case, the downstream flow field must be calculated using the Rankine–Hugoniot (RH) relations.

From the relation between p and ρ for an isentropic process and the definition of the sound speed as $c = \sqrt{\gamma P/\rho}$, the following expression is retrieved:

$$P = P_0\left(\frac{c}{c_0}\right)^{\frac{2\gamma}{\gamma-1}} \tag{30}$$

Riemann invariants are known to be:

$$\begin{aligned} R^- &= u - \frac{2c}{\gamma-1} = \mathrm{const}\left(\text{ along } \frac{\mathrm{d}x}{\mathrm{d}t} = u - c\right), \\ R^+ &= u + \frac{2c}{\gamma-1} = \mathrm{const}\left(\text{ along } \frac{\mathrm{d}x}{\mathrm{d}t} = u + c\right) \end{aligned} \tag{31}$$

Now for the propagation to go from left to right R^- should be uniform in the initial field. We can find the expression for $\mathrm{d}u$ given in (12) as follows. The relation

$$u - \frac{2c}{\gamma-1} = u_0 - \frac{2c_0}{\gamma-1} \tag{32}$$

gives, using (30):

$$\mathrm{d}u = \frac{2c_0}{\gamma-1}\left(\left(\frac{P}{P_0}\right)^{\frac{2\gamma}{\gamma-1}} - 1\right) \text{ with } \mathrm{d}u = u - u_0 \tag{33}$$

Using the polytropic process equation between T and P yields:

$$T = T_0\left(\frac{P}{P_0}\right)^{\frac{\gamma-1}{\gamma}} \tag{34}$$

with $P = P_0 + \mathrm{d}P$.

Acknowledgements This research was supported by the DGA (Direction Générale de l'Armement) and ISAE-SUPAERO. This work was performed using resources from GENCI [CCRT-CINES-IDRIS] (Grant A0122A07178) and from CALMIP (Grant 2022-p1425).

Funding Open access funding provided by ISAE-SUPAERO.

Data Availability Data associated with this work can be made available upon a reasonable request.

References

1. Lechat, T., Emmanuelli, A., Dragna, D., Ollivier, S.: Propagation of spherical weak blast waves over rough periodic surfaces. Shock Waves **31**(4), 379–398 (2021). https://doi.org/10.1007/s00193-021-01024-8
2. Karzova, M.M., Lechat, T., Ollivier, S., Dragna, D., Yuldashev, P.V., Khokhlova, V.A., Blanc-Benon, P.: Effect of surface roughness on nonlinear reflection of weak shock waves. J. Acoust. Soc. Am. **146**(5), 438–443 (2019). https://doi.org/10.1121/1.5133737
3. Cheinet, S., Ehrhardt, L., Broglin, T.: Impulse source localization in an urban environment: time reversal versus time matching. J. Acoust. Soc. Am. **139**(1), 128–140 (2016). https://doi.org/10.1121/1.4938231
4. Aloui, N., Raoof, K., Bouallegue, A., Letourneur, S., Zaibi, S.: Multi-resolution localization method based on time reversal and simulated annealing algorithm. 2013 International Conference on Indoor Positioning and Indoor Navigation, IPIN 2013 (October), pp. 28–31 (2013). https://doi.org/10.1109/IPIN.2013.6817865
5. Liu, M., Cheng, L., Qian, K., Wang, J., Wang, J., Liu, Y.: Indoor acoustic localization: a survey. HCIS **10**, 2 (2020). https://doi.org/10.1186/s13673-019-0207-4
6. Fink, M., Cassereau, D., Derode, A., Prada, C., Roux, P., Tanter, M., Thomas, J.L., Wu, F.: Time-reversed acoustics. Rep. Prog. Phys. **63**(12), 1933–1995 (2000). https://doi.org/10.1088/0034-4885/63/12/202
7. Tanter, M., Thomas, J.L., Coulouvrat, F., Fink, M.: Breaking of time reversal invariance in nonlinear acoustics. Phys. Rev. E Stat. Phys. Plasmas Fluids Relat. Interdiscip. Topics **64**(1), 016602 (2001). https://doi.org/10.1103/PhysRevE.64.016602
8. Lo, K.W., Ferguson, B.G.: Localization of small arms fire using acoustic measurements of muzzle blast and/or ballistic shock wave arrivals. J. Acoust. Soc. Am. **132**(5), 2997–3017 (2012). https://doi.org/10.1121/1.4757737
9. Ben-Dor, G.: Shock Wave Reflection Phenomena, 2nd ed. Springer, Berlin, Heidelberg (2007). https://doi.org/10.1007/978-3-540-71382-1
10. Baskar, S., Coulouvrat, F., Marchiano, R.: Nonlinear reflection of grazing acoustic shock waves: Unsteady transition from von Neumann to Mach to Snell-Descartes reflections. J. Fluid Mech. **575**, 27–55 (2011). https://doi.org/10.1017/S0022112006003752
11. Neumann, J.V.: Oblique reflection of shocks. John von Neumann Collected Work **6**, 239–299 (1963)
12. Colella, P., Henderson, L.F.: The von Neumann paradox for the diffraction of weak shock waves. J. Fluid Mech. **213**, 71–94 (1990). https://doi.org/10.1017/S0022112090002221
13. Bleakney, W., Taub, A.H.: Interaction of shock waves. Rev. Mod. Phys. **21**(4), 584–605 (1949). https://doi.org/10.1103/RevModPhys.21.584
14. Tesdall, A.M., Hunter, J.K.: Self-similar solutions for weak shock reflection. Soc. Ind. Appl. Math. **63**(1), 42–61 (2002). https://doi.org/10.1137/S0036139901383826
15. Skews, B.W., Ashworth, J.T.: The physical nature of weak shock wave reflection. J. Fluid Mech. **542**, 105–114 (2005)
16. Lamouroux, R., Gressier, J., Grondin, G.: A high-order compact limiter based on spatially weighted projections for the spectral volume and the spectral differences method. J. Sci. Comput. **67**(1), 375–403 (2016). https://doi.org/10.1007/s10915-015-0084-6
17. Liu, Y., Vinokur, M., Wang, Z.J.: Spectral difference method for unstructured grids I: Basic formulation. J. Comput. Phys. **216**(2), 780–801 (2006). https://doi.org/10.1016/j.jcp.2006.01.024
18. Persson, P.O.: Shock capturing for high-order discontinuous Galerkin simulation of transient flow problems. 21st AIAA Computational Fluid Dynamics Conference, San Diego, CA, AIAA Paper 2013-3061 (2013). https://doi.org/10.2514/6.2013-3061
19. Cheinet, S., Broglin, T.: Sensitivity of shot detection and localization to environmental propagation. Appl. Acoust. **93**, 97–105 (2015). https://doi.org/10.1016/j.apacoust.2015.01.021
20. Dagallier, A., Cheinet, S., Cosnefroy, M., Rickert, W., Weßling, T., Wey, P., Juvé, D.: Long-range acoustic localization of artillery shots using distributed synchronous acoustic sensors. J. Acoust. Soc. Am. **146**(6), 4860–4872 (2019). https://doi.org/10.1121/1.5138927
21. Hunter, J.K., Brio, M.: Weak shock reflection. J. Fluid Mech. **410**, 235–261 (2000). https://doi.org/10.1017/S0022112099008010
22. Zakharian, A.R., Brio, M., Hunter, J.K., Webb, G.M.: The von Neumann paradox in weak shock reflection. J. Fluid Mech. **422**, 193–205 (2000). https://doi.org/10.1017/S0022112000001609
23. Zabolotskaya, E.A., Khokhlov, R.V.: Quasi-plane waves in the nonlinear acoustic of confined beams. Soviet Phys. Acoust. **15**, 35–40 (1969)
24. Coulouvrat, F., Marchiano, R.: Nonlinear Fresnel diffraction of weak shock waves. J. Acoust. Soc. Am. **114**(4), 1749–1757 (2003). https://doi.org/10.1121/1.1610454
25. Marchiano, R., Coulouvrat, F., Baskar, S., Thomas, J.L.: Experimental evidence of deviation from mirror reflection for acoustical shock waves. Phys. Rev. E Stat. Nonlinear Soft Matter Phys. **76**(5), 1–5 (2007). https://doi.org/10.1103/PhysRevE.76.056602
26. Karzova, M.M., Khokhlova, V.A., Salze, E., Ollivier, S., Blanc-Benon, P.: Mach stem formation in reflection and focusing of weak shock acoustic pulses. J. Acoust. Soc. Am. **137**(6), 436–442 (2015). https://doi.org/10.1121/1.4921681
27. Desjouy, C., Ollivier, S., Marsden, O., Karzova, M., Blanc-Benon, P.: Irregular reflection of weak acoustic shock pulses on rigid boundaries: Schlieren experiments and direct numerical simulation based on a Navier-Stokes solver. Phys. Fluids **28**(2), 027102 (2016). https://doi.org/10.1063/1.4940987
28. Brio, M., Hunter, J.K.: Mach reflection for the two-dimensional Burgers equation. Physica D **60**(1–4), 194–207 (1992). https://doi.org/10.1016/0167-2789(92)90236-G
29. Mouton, C.A.: Transition between regular reflection and Mach reflection in the dual-solution domain. PhD thesis, California Institute of Technology (2007). https://core.ac.uk/download/11809041.pdf

30. Mouton, C.A., Hornung, H.G.: Mach stem height and growth rate predictions. AIAA J. **45**(8), 1977–1987 (2007). https://doi.org/10.2514/1.27460
31. Sparrow, V.W., Raspet, R.: A numerical method for general finite amplitude wave propagation in two dimensions and its application to spark pulses. J. Acoust. Soc. Am. **90**(5), 2683–2691 (1991). https://doi.org/10.1121/1.401863
32. Rasmussen, P., Flamme, G., Stewart, M., Meinke, D., Lankford, J.: Measuring recreational firearm noise. J. Acoust. Soc. Am. **127**, 1794 (2010). https://doi.org/10.1121/1.3384002
33. Sabatini, R., Marsden, O., Bailly, C., Gainville, O.: Three-dimensional direct numerical simulation of infrasound propagation in the Earth's atmosphere. J. Fluid Mech. **859**, 754–789 (2019). https://doi.org/10.1017/jfm.2018.816
34. Richardson, L.F.: The approximate arithmetical solution by finite differences of physical problems involving differential equations, with an application to the stresses in a masonry dam. Philos. Trans. R. Soc. Lond. **210**(459–470), 299–361 (1911). https://doi.org/10.1098/rsta.1911.0009
35. Pierce, A.D.: Acoustics: An Introduction to Its Physical Principles and Applications. Springer, New York (2019). https://doi.org/10.1007/978-3-030-11214-1
36. Deleu, S.: Non-linearities in acoustical shock propagation and interaction. PhD thesis, Université de Toulouse (2023)